A densification mechanism to model the mechanical effect of methane hydrates in sandy sediments

M. De La Fuente[1, 2], J. Vaunat[3], H. Marín-Moreno[2]

[1] National Oceanography Centre, University of Southampton, European Way, Southampton, SO14 3ZH, United Kingdom.
[2] Ocean and Earth Science, University of Southampton, European Way, Southampton SO14 3ZH, UK
[3] Department of Civil and Environmental Engineering, Universitat Politècnica de Catalunya, Barcelona, Spain.

SUMMARY

Recent pore-scale observations and geomechanical investigations suggest the lack of true cohesion in methane hydrate-bearing sediments (MHBS) and propose that their mechanical behavior is governed by kinematic constrictions at pore scale. In this paper, we present a mechanical model for MHBS, which does not rely on physical bonding between hydrate crystals and sediment grains but on the densification effect that pore invasion with hydrate has on the sediment mechanical properties. The Hydrate-CASM extends the critical state model CASM (Clay and Sand Model) by implementing the subloading surface model and introducing the densification mechanism. The model suggests that the decrease of void volume during hydrate formation stiffens the sediment structure and has a similar mechanical effect as the increase of its density. In particular, the model attributes stress-strain changes observed in MHBS to variations in void volume due to hydrate formation and its consequent effect on isotropic yield stress and swelling line slope with hydrate saturation. The model performance is examined against published experimental data from drained triaxial tests performed at different confining stress and with distinct hydrate saturation and morphology. Overall, the simulations capture the influence of hydrate saturation in both the magnitude and trend of the stiffness, shear strength and volumetric response of synthetic MHBS. The results are also validated against those obtained from previous mechanical models for MHBS that use the same experimental data. The Hydrate-CASM performs similarly to the previous models considered although its formulation do not requires any additional parameter, with the exception of one hydrate-related empirical parameter to express changes in the sediment elastic stiffness with hydrate saturation.

KEY WORDS: methane hydrate-bearing sediments; mechanical behavior; densification mechanism; Hydrate-CASM; constitutive modeling.

1. INTRODUCTION

Methane hydrates have drawn international interest as an alternative energy resource to conventional fossil fuels [1-5], and as a major hazard for offshore drilling and gas production operations [6-8], global climate change [9-12] and seafloor instability [13-15]. Quantitative evaluation of the resource potential of gas hydrate reservoirs and of their response to natural and/or human-induced changes in pressure and temperature (P-T) conditions, requires precise knowledge of the hydrate phase change phenomenon and of its effect on the mechanical stability of the reservoir. Due to the operational complexity at preserving the in-situ P-T conditions during MHBS recovery, the mechanical properties of these sediments are generally investigated through geophysical techniques [16-18] and geotechnical testing of synthetic sediments [19-21]. Both geophysical and geotechnical data show that the stiffness, strength, and dilatancy of MHBS tend to increase with increasing hydrate saturation [22, 23]. They also evidence that their mechanical and hydraulic properties drastically change during hydrate dissociation, which may compromise the mechanical stability of the sediment. Thus, hydrate dissociation is likely to trigger small to large-scale deformations in the seabed, including sediment collapse [24] and sliding [25-27]. As a result, dissociation may also induce damage of preexisting offshore infrastructures [28].

Several mechanical models developed for MHBS assume that the increase of strength, stiffness and dilatancy observed in these sediments is mainly governed by bonding or cementation between the hydrate crystal and the sediment grains (Table 1). However, recent pore-scale observations [29-31] and geomechanical investigations [32-34] evidence the lack of true cohesion in MHBS and suggest that the mechanical response of these sediments may not necessarily be governed by sediment bonding/cementation, but rather to kinematic constrictions at pore/grain scale during shearing. In this paper, we develop a new mechanical constitutive model that does not consider hydrate-bonding effects in its formulation but assumes that the reduction of sediment void volume and the increase of sediment elastic stiffness during pore invasion with hydrate can explain the greater mechanical properties observed in MHBS

Table 1: *Notable mechanical models for MHBS considering hydrate-bonding effect*

Model reference	Hydrate-bonding modelling strategy
Klar et al. [35]; Jung et al. [36]; Pinkert and Grozic, [37]; Pinkert et al. [38]	Additional cohesion constituent in the failure criteria
Uchida et al. [39]; Sánchez and Gai [40]; Sánchez et al. [41].	Enlargement of the yield surface by cohesion and dilatation
Sultan and Garziglia et al. [42]	Impediment of the normal consolidation of the sediment and enlargement of the yield surface
Sánchez and Gai [40]; Sánchez et al. [41].De La Fuente et al. [43]	Stress-strain partition between hydrate and matrix in a bonding damage framework (BDM)
Jiang et al. [44]	Attribution of physical bonding properties in discrete element methods (DEM)
Lin et al. [45]	Expansion of the failure envelope in a spatially mobilized plane (SMP) model

The elasto-plastic model Hydrate-CASM extends the formulation of the unified critical state constitutive model CASM [46] by implementing the subloading surface model [47] and introducing the densification mechanism. The subloading surface, which has been successfully used in previous mechanical models for MHBS [39, 40, 44, 48], allows capturing irrecoverable plastic strains inside the yield surface. The densification mechanism suggests that the decrease of the available void ratio of the host sediment during hydrate formation stiffens its structure and has a similar mechanical effect as the increase of the sediment density. In particular, the densification mechanism attributes the stress-strain changes observed in MHBS to variations in the available void ratio, isotropic yield stress and swelling line slope of the host sediment with hydrate saturation.

The Hydrate-CASM is applied here to robust and well-described published experimental data [19, 21] that cover the most relevant conditions related to MHBS behavior, including a wide range of hydrate saturations, several hydrate morphologies and confinement stress. These data have also been used in the calibration of previous mechanical models developed for MHBS [e.g., 39, 40, 48-50], which give us the opportunity to compare and validate our results. The model performance is found satisfactory over a wide range of test conditions and evidence the capability of the Hydrate-CASM model at capturing both the trend and magnitude of the stress-strain and the volumetric response of synthetic MHBS. Overall, the good matching of our results with the outputs obtained from previous mechanical models for MHBS evidences that the experimental data examined in this paper can be simply reproduced by (i) considering the mechanical effect of the reduction of sediment void volume due to pore invasion with hydrate and (ii) modifying the sediment elastic stiffness according to hydrate saturation. In addition, our results also show that accounting for the different initial porosities of the set of host specimens used to produce cementing and pore-filling MHBS allows capturing the experimental data without using any empirical parameters related to hydrate morphology.

2. CASM MODEL

The Hydrate-CASM extends the formulation of the constitutive model CASM developed by Yu [46]. The CASM model is selected here because of its simplicity and flexibility in describing the shape of the yield surface as well as its proven ability to predict the mechanical behavior of sand, the most likely target for the commercial exploitation of hydrates [51]. The critical state model CASM is formulated in terms of the state parameter [52] and the spacing ratio concept, and uses a non-associated flow rule, which is particularly suitable to simulate the behavior of granular sediments like those examined in this paper [53, 54]. All the parameters used in the formulation are listed and defined in Table 2.

Table 2. CASM and Hydrate-CASM parameters. Subscript h refers to hydrate-bearing sediment properties and bold symbols denote tensors. Note that e_{ah}, v_h , p_{o_h} and κ_h recover the hydrate-free parameters e, v, p_0 and κ when S_h=0.

Model parameters		***Description***
Stress	P_p	Pore pressure
	$\boldsymbol{\sigma}$	Cauchy total stress tensor
	$\mathbf{I}$	Identity matrix
	$\boldsymbol{\sigma}'$	Cauchy effective stress tensor, $\boldsymbol{\sigma}' = \boldsymbol{\sigma} - P_p\mathbf{I}$
	$\boldsymbol{\sigma_c}$	Confining total stress
	$\boldsymbol{\sigma'}_{\boldsymbol{c}}$	Confining effective stress, $\boldsymbol{\sigma'}_{\boldsymbol{c}} = \boldsymbol{\sigma_c} - P_p$
	p	Mean stress, $p = {}^1/_3\,(\sigma_1 + \sigma_2 + \sigma_3\,)$
	q	Deviatoric stress, $q = \sigma_1 - \sigma_3$
	p'	Mean effective stress, $p' = p - P_p$
	η	Stress ratio $\eta = q/p'$
Strain	$\boldsymbol{\varepsilon}$	Total infinitesimal strain tensor
	$\boldsymbol{\varepsilon}^e$	Elastic strain tensor
	$\lvert d\varepsilon^p \rvert$	Norm of the incremental plastic strain vector
	ε_v^p	Plastic volumetric strain, $\varepsilon_v^p = \varepsilon_1^p + \varepsilon_2^p + \varepsilon_3^p$
	ε_q^p	Plastic deviatoric strain, $\varepsilon_q^p = \frac{2}{3}(\varepsilon_1^p - \varepsilon_3^p)$
	V_t	Total volume

Volumetric ratios	V_s	Volume of mineral grains
	V_h	Volume of hydrate
	V_v	Potential void volume, $V_v = V_t - V_s$
	V_a	Available void volume, $V_a = V_v - V_h$
	e	Void ratio of the host sediment, $e = V_v/V_s$
	S_h	Hydrate saturation, $S_h = V_h/V_v$
	e_h	Hydrate ratio, $e_h = V_h/V_s = S_h e$
	e_{a_h}	Available void ratio of the hydrate-bearing sediment, $e_{a_h} = e(1 - S_h)$
	v	Specific volume, $v = 1 + e$
	v_h	Hydrate-CASM equivalent specific volume , $v_h = \ v - e_h$
Critical state parameters	λ	Slope of the normal compression and critical state lines in the $v - ln(p')$ space
	M	Critical state stress ratio: slope of critical state line in the $p' - q$ space
	p_0	Isotropic yield stress of the host sediment
	p_{0_h}	Isotropic yield stress of the hydrate-bearing sediment
	p'_x	Mean effective stress at critical state
	Γ	Specific volume at critical state with p' of 1 KPa
Elastic parameters	κ	Host sediment swelling (reloading-unloading) line slope
	κ_h	MHBS swelling (reloading-unloading) line slope
	ν	Poisson's ratio
	K	Elastic bulk modulus
	G	Elastic shear modulus
	$\boldsymbol{D}^e$	Elastic stiffness tensor
CASM parameters	n	Stress-state coefficient: yield surface shape parameter
	r	Spacing ratio, $r = p_0' \,/p'_x$
	ξ	State parameter
	ξ_r	Reference state parameter, $\xi_r = (\lambda - \kappa)lnr$
Subloading parameters	p_{0_s}	Isotropic yield stress of the subloading surface
	R	Subloading surface ratio, $R = p_{0_S}/p_0$
	u	Subloading parameter controlling plastic deformations before yielding
Plastic parameters	φ	Size parameter
	$\boldsymbol{\chi}$	Vector of hardening (2 components: p_{0_h} and R)
	H	Hardening modulus
	λ^p	Plastic multiplier
Empirical parameters	κ_{rf}	Swelling line reduction factor

2.1. State parameter concept

The state parameter (Eq. 1) is defined in the $v - ln(p')$ space as the vertical distance between the void ratio at the current state and that at the critical state for a given mean effective stress (Figure 1a):

$$\xi = v + \lambda\, ln(p') - \Gamma \quad (1)$$

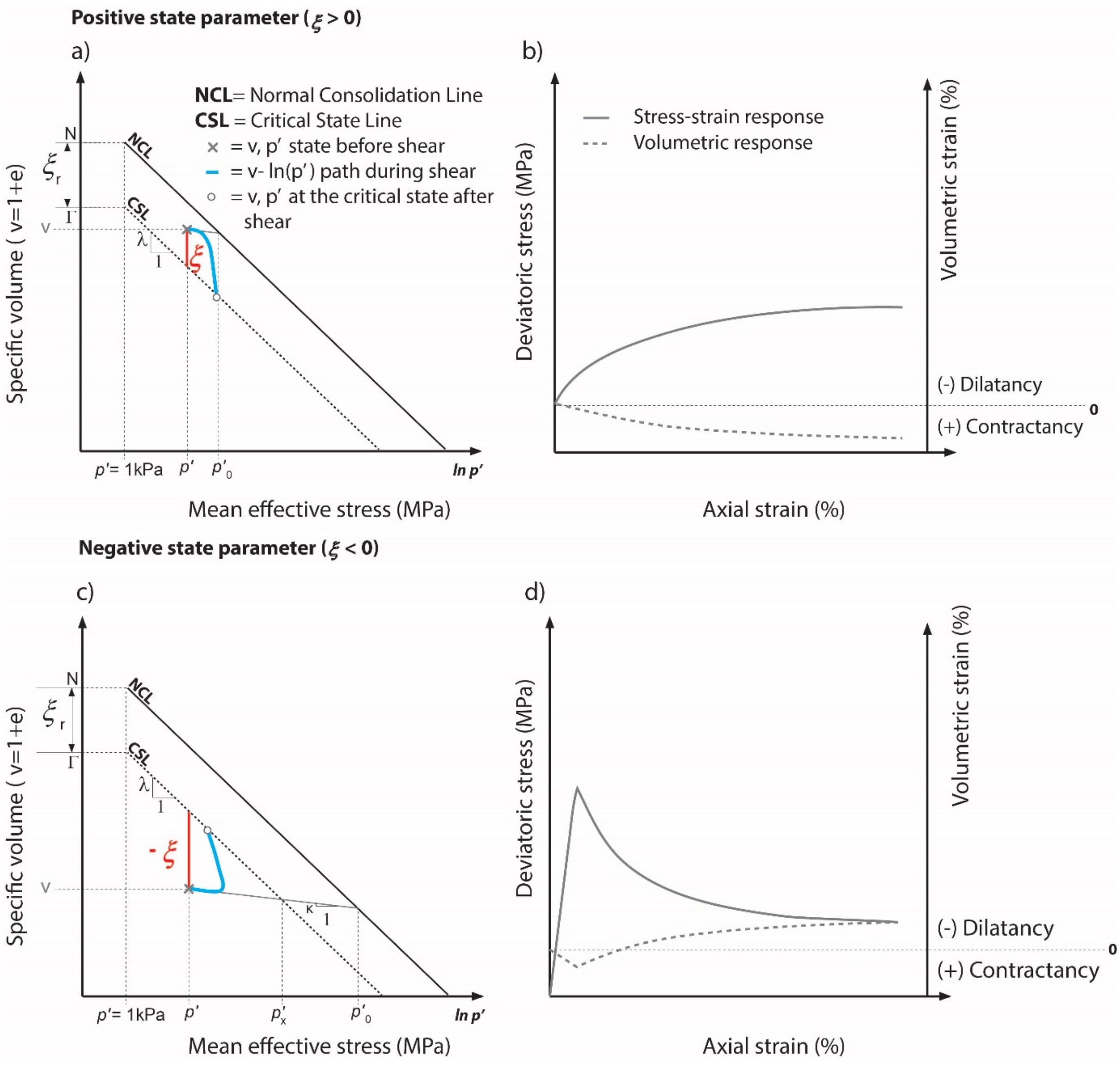

Figure 1: CASM framework. Graphical representation of the CASM parameters and qualitative mechanical response of sediments subjected to triaxial shear with (a, b) positive and (c, d) negative values of ξ. After [46].

The magnitude and sign of this parameter play a key role in understanding the densification mechanism introduced in this paper. The state parameter adopts positive values when the sediment void ratio is located above the critical state line (CSL) (as in loose sand; Figure 1a), and negative ones when located below it (as in dense sand; Figure 1c). Sediments with a positive value of ξ and subjected to triaxial shear tend to show hardening on the $p' - q$ stress space and contractancy as volumetric response (Figure 1b). Instead, sediments with a negative value of ξ show a distinctive peak in the deviatoric stress followed by softening before the critical state is achieved, and dilatancy dominates its volumetric response (Figure 1d).

2.2. CASM yield function

A total of seven model parameters are required to define the original CASM formulation. Five of which (λ,M, Γ, κ and ν), are the same as those in the Cam Clay model [55,56], and the two additional parameters, denoted by n and r, are used to specify the geometrical properties of the yield function. For a general stress state, the CASM yield function is expressed as:

$$f = \left(\frac{q}{Mp'}\right)^n + \frac{1}{ln(r)} ln\left(\frac{p'}{p'_0}\right) \quad (2)$$

Where n governs the shape of the yield surface and r controls its intersection with the critical state line. Particular combinations of n and r allow the intersection between the critical state line and the yield surface to not necessarily occur at the maximum deviatoric stress (Figure 2) as happens in Cam-Clay type models. This allows the CASM model to predict local peaks in the deviatoric stress on the left side of the critical state condition, feature that is widely observed in geotechnical testing of sand [57, 58]. Certain values of n and r can also recover the yield surface function of the standard and modified Cam-clay models [46].

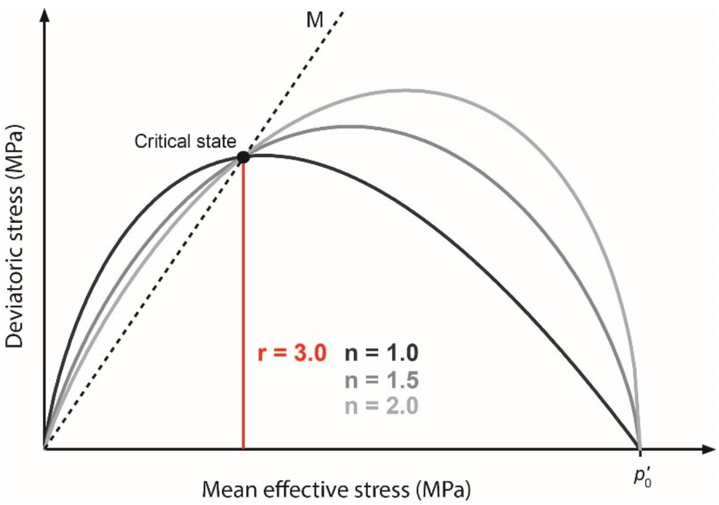

Figure 2: Influence of n and r in the shape and size of the yield surface. Note the presence of local peaks in the deviatoric stress on the left side of the critical state condition. After [46].

Within the yield surface, the behavior is assumed isotropic and elastic, with the elastic volumetric stress-strain relationship governed by the bulk modulus K (Eq. 3a) and the elastic shear by the shear modulus G (Eq. 3b):

$$K = \frac{(1+e)p\prime}{\kappa} \text{ (3a)}$$

$$G = \frac{3K(1-2\nu)}{2(1+\nu)} \text{ (3b)}$$

2.3. Stress-dilatancy relation and plastic potential

The CASM model uses a non-associated flow rule that follows the stress-dilatancy law proposed by Rowe [59], which has been applied with success at describing the deformation of sands and granular materials [46], as well as to simulate the response of MHBS [32, 33].:

$$\frac{d\varepsilon_v^p}{d\varepsilon_q^p} = \frac{9(M-\eta)}{9+3M-2M\eta} \text{ (4)}$$

By integrating equation (4), the CASM plastic potential function is obtained as:

$$g = 3M ln\left(\frac{p\prime}{\varphi}\right) + (3+2M) ln\left(\frac{2q}{p\prime} + 3\right) + (M-3) ln\left(3 - \frac{q}{p\prime}\right) \text{ (5)}$$

Whose expression does not depend on the hardening parameters and where φ is a size parameter controlling the size of the plastic potential which passes through the current stress state $(p' - q)$.

2.4. Hardening parameters

Similar to Cam-clay type models, the CASM model assumes isotropic changes in the isotropic yield stress controlled by the incremental plastic volumetric deformation, so that:

$$dp_0' = \frac{(1+e)\, p_0'}{\lambda-\kappa} d\varepsilon_v^p \text{ (6)}$$

3. HYDRATE-CASM FORMULATION

The Hydrate-CASM extends the formulation of the CASM model [46] by implementing the subloading surface model [47] and introducing the densification mechanism. We note that material parameters e, ν, p'_0 and κ presented in equations 1 to 5 read as e_{ah}, ν_h , p'_{0_h} and κ_h in the presence of hydrate within the sediment.

3.1. Hydrate-CASM subloading function

It is widely recognized that plastic strains can develop for stress states inside the yield surface; its interior is not a purely elastic domain. This feature results in a smooth transition between the elastic and the plastic response of soils [60, 61]. González [62] shows that the CASM yield function reproduces well the residual soil strength, but generally over-estimates the elastic strains and predicts unrealistic sharp transitions between the elastic and elastoplastic states. The subloading surface concept [47] is implemented in the present formulation to account for pre-yield plasticity that allows capturing a smoother transition between elastic and plastic behavior, and a more accurate volumetric response of MHBS. This model assumes the existence of a subloading surface that expands/contracts inside the general yield surface keeping its same shape. The Hydrate-CASM subloading function is derived from equation 2 as:

$$f = \left(\frac{q}{Mp\prime}\right)^{n} + \frac{1}{ln(r)} ln\left(\frac{p\prime}{Rp'_{0_h}}\right) \quad (7)$$

Where R controls the size of the subloading surface (Table 2) and recovers the original CASM yield function for values equal to 1. The evolution of R is controlled by the norm of the incremental plastic strain vector and the subloading parameter (u):

$$dR = -ulnR|d\boldsymbol{\varepsilon}^{p}| \quad (8)$$

3.1.1. Plastic strain

The constitutive equation that characterizes an elasto-plastic material can be expressed as the following stress-strain relationship:

$$d\boldsymbol{\sigma}' = \boldsymbol{D}^{e} d\boldsymbol{\varepsilon}^{e} = \boldsymbol{D}^{e}(d\boldsymbol{\varepsilon} - d\boldsymbol{\varepsilon}^{p}) \quad (9a)$$

With:

$$\boldsymbol{D}^e = \begin{bmatrix} K+\frac{4}{3}G & K-\frac{2}{3}G & K-\frac{2}{3}G & 0 & 0 & 0 \\ K-\frac{2}{3}G & K+\frac{4}{3}G & K-\frac{2}{3}G & 0 & 0 & 0 \\ K-\frac{2}{3}G & K-\frac{2}{3}G & K+\frac{4}{3}G & 0 & 0 & 0 \\ 0 & 0 & 0 & G & 0 & 0 \\ 0 & 0 & 0 & 0 & G & 0 \\ 0 & 0 & 0 & 0 & 0 & G \end{bmatrix} \text{(9b)}$$

$$d\boldsymbol{\varepsilon}^{\boldsymbol{p}} = d\lambda^p \frac{\partial g}{\partial \boldsymbol{\sigma}'} \text{(9c)}$$

The elastoplastic regime is reached when the stress state lies on the Hydrate-CASM yield surface. For the stress state to remain on it at any plastic loading, the consistency condition must be satisfied:

$$df(\boldsymbol{\sigma}', \boldsymbol{\chi}) = 0 \text{ (10)}$$

By linearizing the consistency condition, df can be rewritten as:

$$df = \left(\frac{\partial f}{\partial \boldsymbol{\sigma}'}\right)^T d\boldsymbol{\sigma}' + \left(\frac{\partial f}{\partial \boldsymbol{\chi}}\right)^T d\boldsymbol{\chi} = 0 \text{ (11a)}$$

with:

$$\frac{\partial f}{\partial \boldsymbol{\sigma}'} = \frac{\partial f}{\partial p'}\frac{\partial p'}{\partial \boldsymbol{\sigma}'} + \frac{\partial f}{\partial q}\frac{\partial q}{\partial \boldsymbol{\sigma}'} \text{ (11b)}$$

$$\frac{\partial f}{\partial \chi} = \left(\frac{\partial f}{\partial {p'_o}_h} + \frac{\partial f}{\partial R}\right) \text{ (11c)}$$

By solving equations 9c and 10 the plastic multiplier is classically obtained as:

$$d\lambda^p = \frac{\left(\frac{\partial f}{\partial \boldsymbol{\sigma}'}\right)^T \boldsymbol{D}^e d\boldsymbol{\varepsilon}}{H + \left(\frac{\partial f}{\partial \boldsymbol{\sigma}'}\right)^T \boldsymbol{D}^e \frac{\partial g}{\partial \boldsymbol{\sigma}'}} \text{ (12)}$$

where:

$$H = -\left(\frac{\partial f}{\partial {p'_o}_h}\frac{\partial {p'_o}_h}{\partial d\varepsilon_v^p} + \frac{\partial f}{\partial R}\frac{\partial R}{\partial |d\boldsymbol{\varepsilon}^{\boldsymbol{p}}|}\right)\delta^T \frac{\partial g}{\partial \boldsymbol{\sigma}'} \text{ (12a)}$$

$$\delta^T = \{1,1,1,0,0,0\} \text{ (12b)}$$

3.2. Densification mechanism

In nature, variations in the sediment void volume may result from two competing and interdependent processes: (i) mineral precipitation or dissolution (which compares here to hydrate formation and dissociation, respectively) and (ii) mechanical compaction or dilation under pressure [63]. In particular, mineral precipitation in pores reduces the sediment available void volume without experiencing mechanical compaction [64 and 65] and has a significant effect on its hydraulic and mechanical properties [e.g., 63, 66].

Figure 3 examines qualitatively the effect of sediment density or void ratio on the magnitude of ξ and the corresponding mechanical behavior of the sediment under triaxial shear.

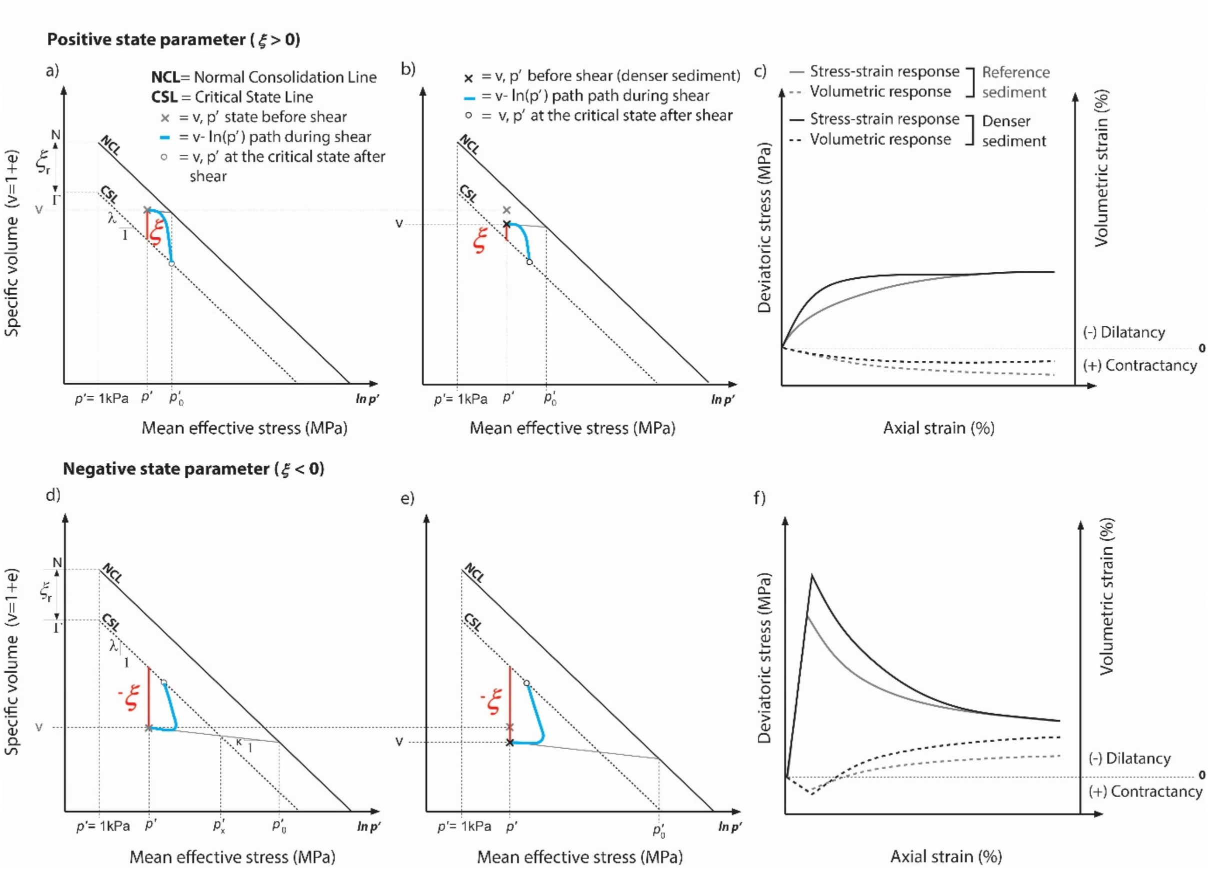

Figure 3: Effect of the increase in the sediment density on the magnitude of ξ and the corresponding stress-strain behavior of the sediment under triaxial shear. (a,d) Initial ξ for the reference sediments, (b, e) evolution of ξ due to densification, and (c, f) computed stress-strain response of the sediment at different densities.

For a reference sediment with positive ξ (grey cross in Figure 3a and 3b), an increase in density or a reduction of the void ratio reduces the vertical distance between the current state and the CSL (black cross in Figure 3b). Thus, during shear, the model predicts less hardening and contractancy than that observed on the reference sediment (Figure 3c). For a reference sediment with negative ξ (grey cross in Figure 3d and 3e), an increase in density increases the distance of the current state from the CSL (black cross in Figure 3e), and consequently, during shear, the model predicts a higher peak strength and greater dilatancy than that observed on the reference sediment (Figure 3f).

Figure 3 shows that variations in ξ related to an increase in sediment density produce a similar mechanical response than those observed in sediments with increasing hydrate saturation (i.e., greater strength and dilatancy, or less contractancy, compared to the sediment without hydrate). Thus, we suggest that the occurrence of hydrate as a solid phase invading the voids of the hosting sediment may have a similar mechanical effect than the increase of the host sediment density. Alike Gupta et. al. [67], the Hydrate-CASM formulation conceptually divides the sediment void-space into potential void volume (V_v) and available void volume (V_a) (Figure 4). The potential void volume is the space between the mineral grains of the sediment and includes the available void volume for fluid flow and storage and the hydrate volume.

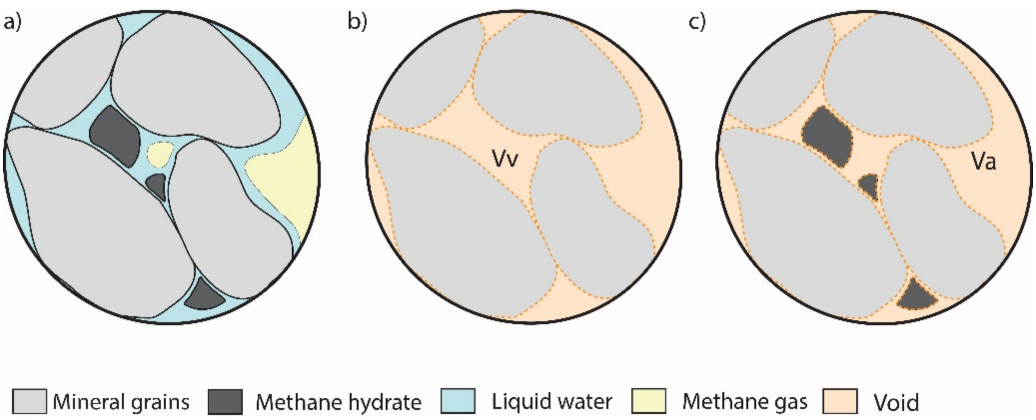

Figure 4: (a) Pore-scale phase distribution in MHBS, (b) potential void volume and (c) available void volume. Note that $V_v = V_a$ for S_h=0.

To introduce the densification effect that pore invasion by hydrate has on the mechanical response of the sediment; the Hydrate-CASM uses the available void ratio left after hydrate formation (Eq.13) to derive the mechanical properties of the sediment.

$$e_{a_h} = e(1 - S_h) = e - e_h \quad (13)$$

From where, variations in ξ with hydrate saturation can be derived as:

$$d\xi = de_h \quad (14)$$

In addition to the reduction of the host sediment available void ratio, the presence of hydrate also enhances the sediment stiffness [16, 22, 23]. We represent the stiffening effect of hydrate on the elastic response of the sediment by the following explicit dependency between κ and S_h:

$$\kappa_h = \kappa\, \kappa_{rf} \quad (15)$$

With:

$$\kappa_{rf} = \begin{cases} 1, & S_h = 0 \\ 3{S_h}^2 - 2.68 S_h + 0.9934, & 0 < S_h \leq 0.42 \\ 0.397, & S_h > 0.42 \end{cases} \quad (16)$$

Equation 16 is obtained empirically by calibrating the experimental data of three synthetic sediments with hydrate saturations ranging from 24.2% to 53.1% (data examined in section 4.2). This empirical relation needs validation for other sediments and hydrate saturations outside the range used for its determination.

The decrease of κ in MHBS has been recently observed in experimental high-pressure oedometer tests [68]. In our formulation the use of κ_{rf} compensates for spurious changes of K (Eq. 3a) when reducing the sediment available void ratio with increasing S_h. If neglecting the hydrate-related stiffening effect suggested in Eq.15, the Hydrate-CASM is still capable of reproducing a close solution to the experimental results (purple line in Figure 5b). However, the use of κ_h adopted in this work leads to a better fit of the elastic response and the peak strength of synthetic hydrate-bearing sediments subjected to triaxial shear (red line in Figure 5b).

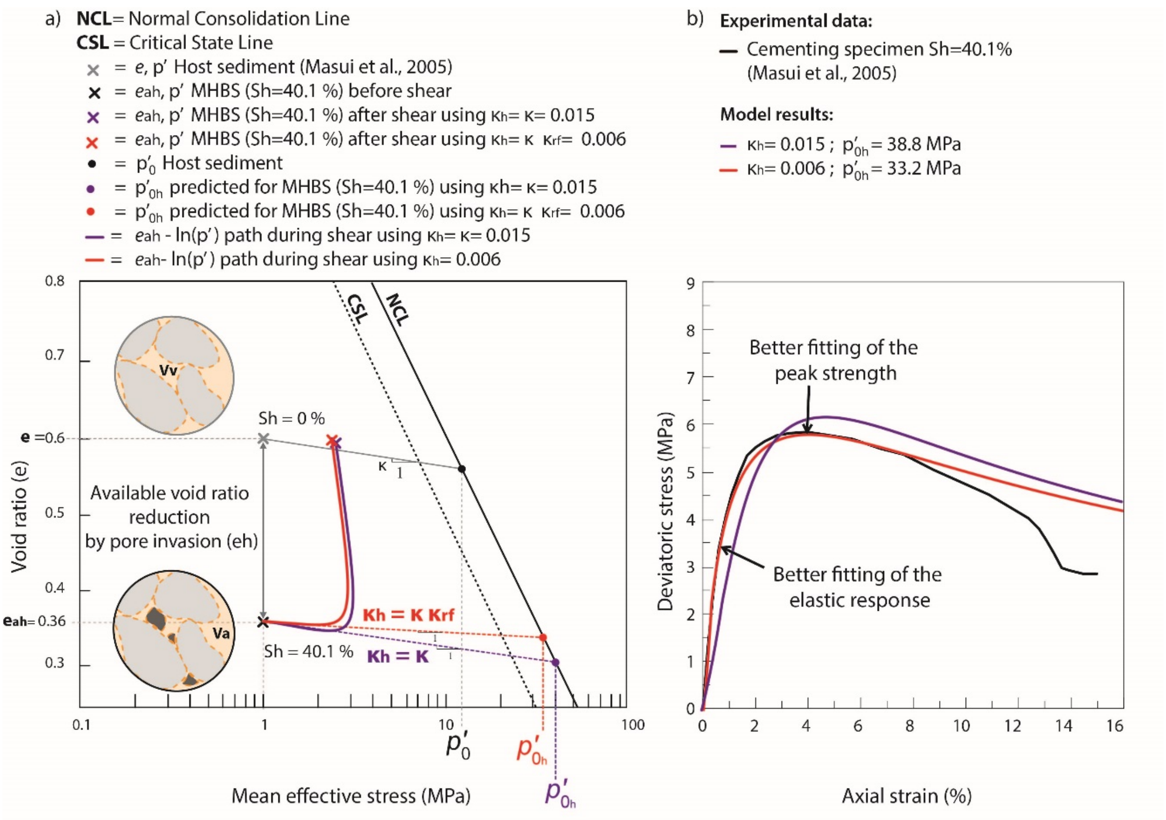

Figure 5: Influence of the densification and stiffening effects caused by hydrate formation in pores at (a) predicting the isotropic yield stress of MHBS and at (b) capturing its mechanical response under triaxial shear (experimental data from [19]). Note that the $e_{ah} - \ln(p')$ paths are plotted here in terms of available void ratio.

As a result of both the decrease of the host sediment available void ratio and the increase of its stiffness during hydrate formation, a greater isotropic yield stress can be deduced graphically in the $v - \ln(p')$ space by projecting e_{ah} on the normal consolidation line (NCL) of the host sediment following the κ_h slope (Figure 5a), so that:

$$p'_{0_h} = exp\left(\frac{e_h}{\lambda-\kappa_h}\right) p_0'^{\left(\frac{\lambda-\kappa}{\lambda-\kappa_h}\right)} \quad (17a)$$

Where changes in $p'_{0_h}$are computed through dp'_0, which reads:

$$dp'_0 = \frac{(1+e_{ah})p'_0}{\lambda-\kappa} d\boldsymbol{\varepsilon}_v^p \quad (17b)$$

3.2.1. MHBS critical state

To evaluate the influence of the densification mechanism due to hydrate formation in the critical state of the sediment, Figure 6b relates the potential void ratio of the host sediment (e) with the isotropic yield stress predicted after hydrate formation (p'_{0h}).

Figure 6a shows the procedure to obtain the isotropic yield stress of the MHBS (p'_{0h}), for which the sediment with hydrate is considered mechanically denser ($e_{ah} < e$) and stiffer ($\kappa_h < \kappa$) than the corresponding host sediment. When relating p'_{0h} with the potential void ratio of the sediment (e), both the NCL and CSL move to the right in the $v - \ln(p')$ space (Figure 6b). Thus, for a given S_h the model predicts a normal consolidation line NCLh that is parallel to that for the host sediment (NCL) and that keeps a vertical distance from the CSLh equal to ξ_r (Table 2).

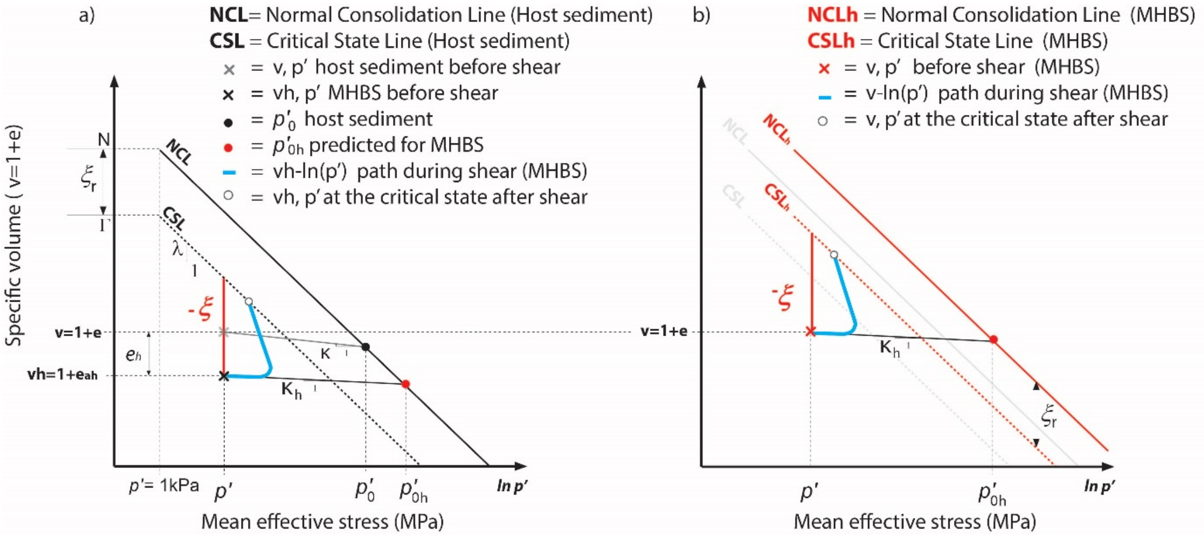

Figure 6: Effect of the densification mechanism at predicting (a) p'_{0h} and (b) shifting both NCL and CSL.

3.2.2. Hydrate dissociation phenomena

Several experimental studies [69-74], and field observations [7-9, 13, 14] have demonstrated the impact of hydrate dissociation in the mechanical properties of MHBS. Hydrate dissociation occurs when the P-T and salinity conditions of the system are outside the hydrate stability zone. In the case of hydrate dissociation, the available porosity of the sediment increases proportionally to the volume of hydrate dissociated, which in turn increases the sediment permeability and reduces its stiffness and strength [22, 75]. Consequently, stress changes and mechanical deformation might be expected during specific conditions of hydrate dissociation. This aspect is integrated in the model since equations 13 to 17b predict an increase in both e_{a_h} and κ_h, as well as a decrease in p'_{0_h} with decreasing S_h.

Figures 7 and 8 examine qualitatively the performance of the model in two different scenarios of thermal-induced hydrate dissociation under constant effective stress.

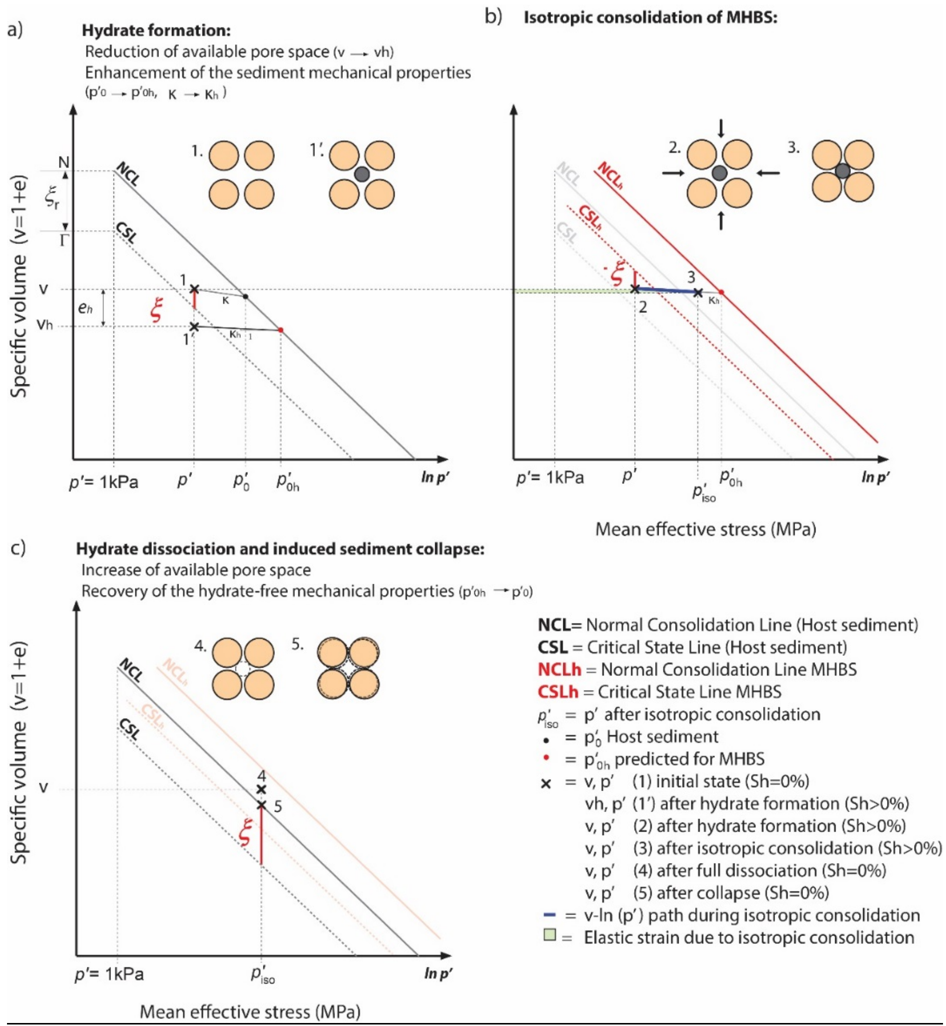

Figure 7: Qualitative analysis of sediment collapse due to hydrate dissociation after isotropic consolidation. (a) Evolution of the host sediment available porosity and increase of the isotropic yield stress due to hydrate densification effect. (b) Prediction of the NCL_h and CSL_h characterizing the MHBS and $v - \ln(p')$ evolution during isotropic consolidation. (c) Sediment collapse induced by hydrate dissociation under constant effective stress. Pore-scale diagrams schematically depict the effect of hydrate formation, mechanical loading, hydrate dissociation and collapse on the porous structure.

Figure 7 shows the ability of the model at predicting sediment collapse induced by hydrate dissociation after isotropic consolidation. Upon hydrate dissociation, the sediment is assumed to recover the mechanical properties of the host sediment (i.e., NCL and CSL). Then, and as observed by Yoneda's et al. [68] observations, if after the hydrate dissociation the $v-\ln(p')$ state of the sediment is located in a mechanically inadmissible stress state (point 4 in Figure 7c) the model can predict sediment collapse until reaching a normally consolidated state (point 5 in Figure 7c).

Figure 8 examines the deformation properties of a hydrate-free specimen and a dissociated MHBS during triaxial shear. Initially, both sediments are isotropically consolidated up to p'_{iso} (Figures 8a and 8c). After consolidation, the MHBS is subjected to dissociation under constant effective stress (point 3, Figure 8d), so that the mechanical properties of the host sediment are recovered (i.e., NCL and CSL, Figure 8d). Then, both sediments are sheared under drained conditions. In agreement with experimental observations in synthetic MHBS subjected to dissociation after isotropic consolidation [75], our model predicts a lower failure strength for the MHBS after dissociation than that observed in the host sediment during shear (Figure 8e).

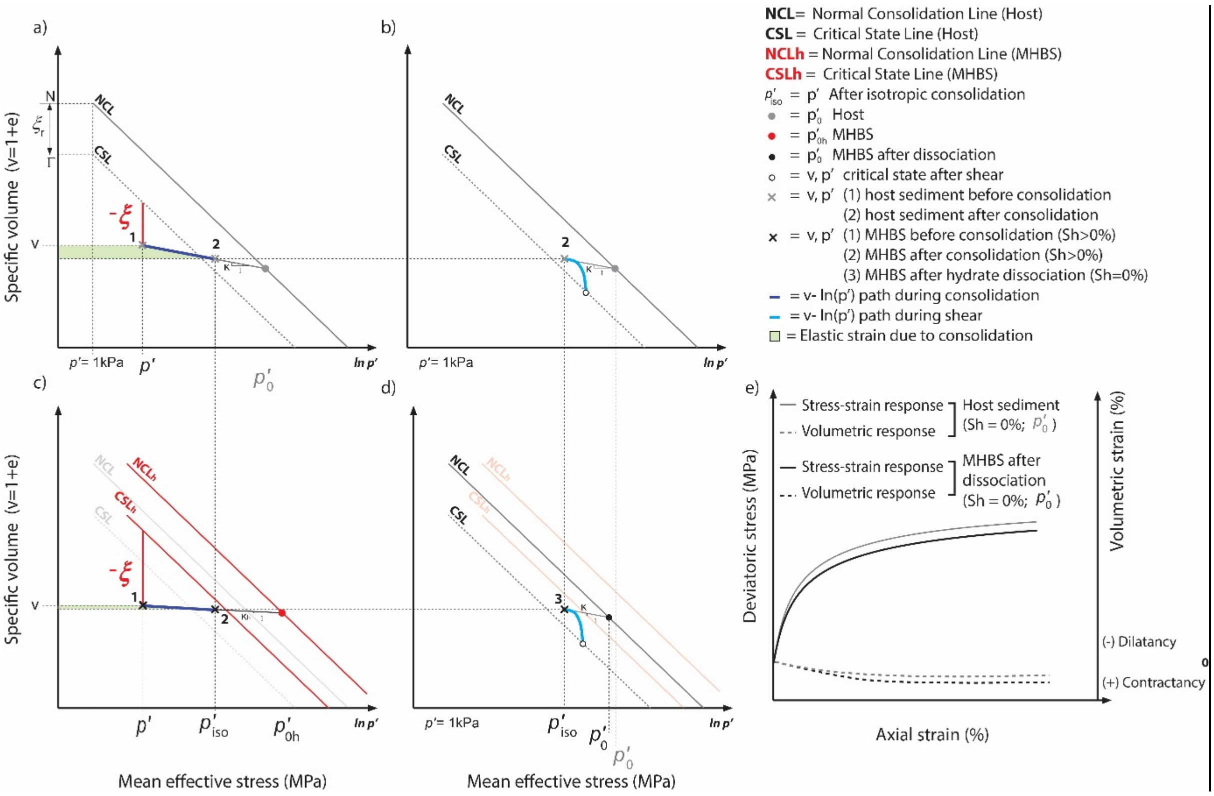

Figure 8: Qualitative analysis of changes in the stress-strain response of both host and dissociated MHBS subjected to shear after isotropic consolidation. Evolution of the $v - ln(p')$ state during (a, c) isotropic consolidation, (b) triaxial shear of the host sediment and (d) hydrate dissociation followed by triaxial shear of the dissociated MHBS. (e) Computed mechanical response during triaxial shear.

4. HYDRATE-CASM PERFORMANCE

Triaxial tests at constant hydrate saturation provide very useful information to understand the influence of hydrate saturation on the mechanical behavior of MHBS. Two sets of stress-strain data from published triaxial tests are used here to evaluate the model performance. The selected experimental data report the mechanical behavior of synthetic MHBS subjected to drained triaxial shear at different confining effective stress, hydrate morphology and saturation. This data have been widely used to calibrate previous mechanical models developed for MHBS, which allows us to compare the model results and validate our formulation.

4.1. Modeling of Masui's et al. (2005) experimental tests

Masui et al. [19] conducted several triaxial tests on synthetic MHBS at different hydrate saturations and both pore-filling and cementing hydrate morphologies. Toyoura sand specimens with slightly different porosities (Table 3) were used as host sediments for the preparation of the hydrate-bearing sand. Prior to forming hydrate, the host sediments were isotropically consolidated up to 1 MPa of confining effective stress. Subsequently, the ice-seed method and the partial water saturation method were employed to produce hydrates with dominant pore-filling and cementing morphologies, respectively. After hydrate formation, the hydrate-bearing sand specimens were sheared at a constant rate of 0.1 % min^{-1} in drained conditions.

Table 3. Physical properties of Toyoura sand used as host sediment in Masui et al. [19].

	Specimens used to form hydrate with cementing morphology	Specimens used to form hydrate with pore-filling morphology
Diameter/height (mm)	50/100	50/100
Density (g/cm^3)	1.74–1.92	1.77–1.78
Porosity (%)	36.3–38.7	42.3–42.9

The set of critical state parameters for the Toyoura sand (Table 4) have been calibrated using the stress-strain curve and the volumetric response of the specimen used for the synthetic formation of cementing hydrate morphology and tested without hydrate (S_h=0% in Figure 9c). Henceforward, these specimens will be called "cementing specimen without hydrate". Similarly, the specimens used to form hydrate with pore filling morphology will be called "pore-filling specimen without hydrates". For the calibration process, values used in previous publications that also model the mechanical response of Toyoura sand have been considered as a reference [e.g., 39, 41, 45]. In addition, the different porosities of 0.6 and 0.75 reported for the host cementing and pore-filling specimens respectively, have been considered in the modelling (Table 4).

Table 4. Input parameters for modeling the host sediment used by Masui et al. [19] in triaxial tests.

Model parameters									
e	λ	M	$p'_0(MPa)$	κ	υ	n	r	$p'_{0_s}(MPa)$	u
Specimens used to form hydrate with cementing morphology ($S_h = 0\%$)									
0.6	0.22	1.17	12	0.015	0.1	2.5	1.7	3.5	20
Specimens used to form hydrate with pore-filling morphology ($S_h = 0\%$)									
0.75	0.22	1.17	5.3	0.015	0.1	2.5	1.7	3	20

Figure 9 shows the model results for Masui's et al. [19] triaxial tests. Overall, our results show that Hydrate-CASM successfully captures the trend and magnitude of the mechanical response of MHBS subjected to shear, showing an increase in stiffness, shear strength, and dilatancy with increasing S_h (Figures 9c to 9f). The model outputs fit particularly well the volumetric response of the cementing specimens (Figure 9e) as well as the rate of increase observed in the peak strength with S_h (Figure 9f). However, they underestimate the maximum deviatoric stress of the cementing specimen with S_h=55.1% (Figure 9c) and slightly overestimate the maximum deviatoric stress of the pore-filling specimen with S_h=26.4% (Figure 9d) and the volumetric response of the pore-filling sediment with S_h=40.9% (Figure 9e).

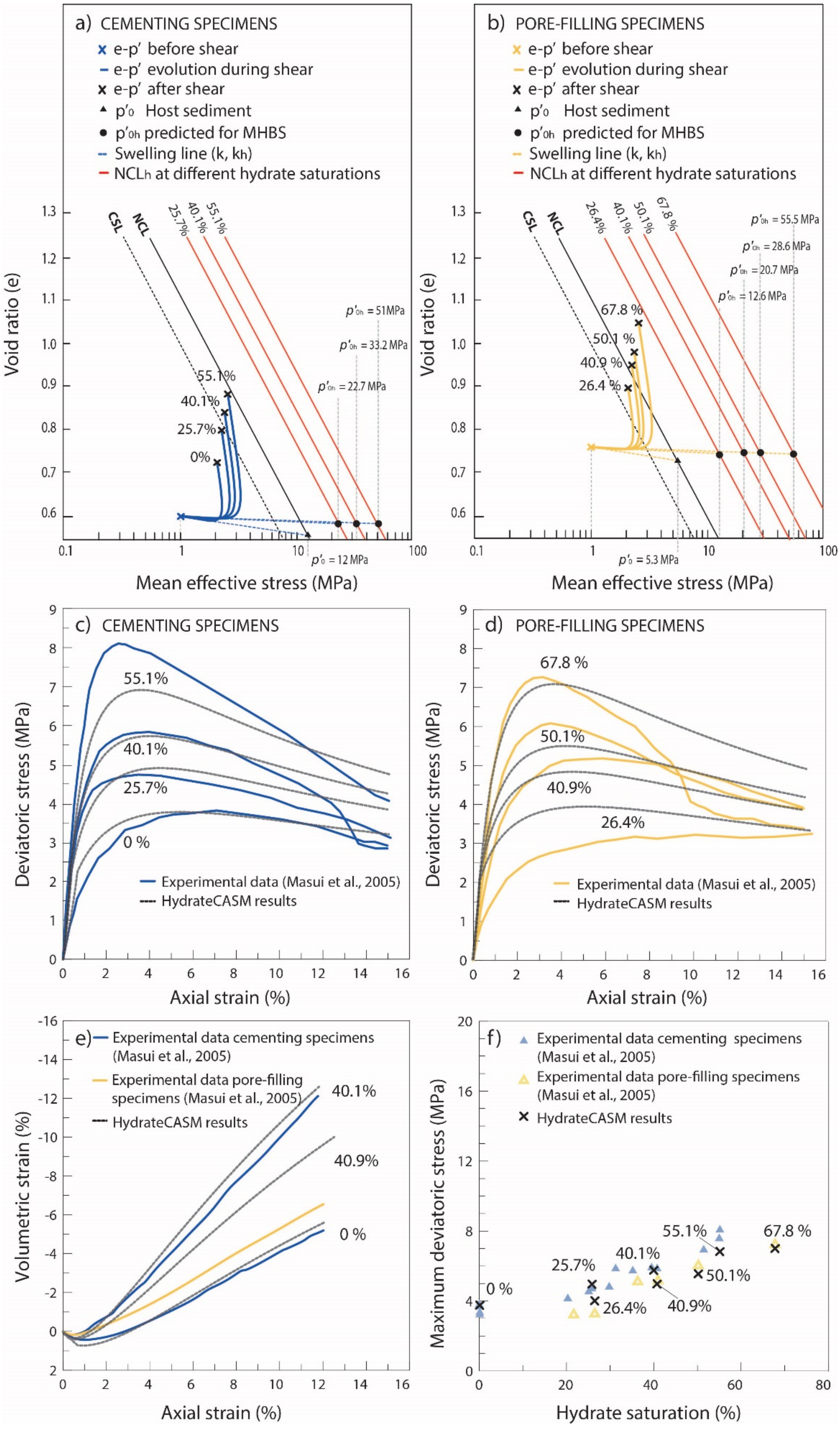

Figure 9: (a,b) Effect of the host sediment void ratio and the hydrate saturation at shifting the NCL of the sediment. Stress-strain behavior predicted during triaxial shear for (c) cementing

and (d) pore-filling specimens. (e) Volumetric response under triaxial shear of cementing specimens with S_h= 0% and 40.1% and pore-filling specimens with S_h=40.9%. (f) Comparison of the sediment peak strength at different hydrate saturations predicted by the model and the corresponding experimental measurement. Percentages indicated in the figure correspond to hydrate saturations.

Previous mechanical models for MHBS that also modelled Masui's et al. [19] data [e.g., 39, 41, 50] assume that the differences in strength and dilatancy observed between the cementing and pore-filling specimens for a given hydrate saturation are controlled by hydrate morphology. However, Masui et. al. [19] state that if the pore hydrate saturation is the same in both types of specimens (e.g., Sh≈ 40% in Figures 9c and 9d), shear strength becomes higher for the specimen with lower porosity. The similarity between the results from previous models and those obtained with the Hydrate-CASM (Figure 10), which does not consider mechanical contributions related to hydrate morphology, suggests that the different mechanical behavior between cementing and pore-filling specimens can be alternatively reproduced considering the different porosity reported for each set of host specimens (Table 3).

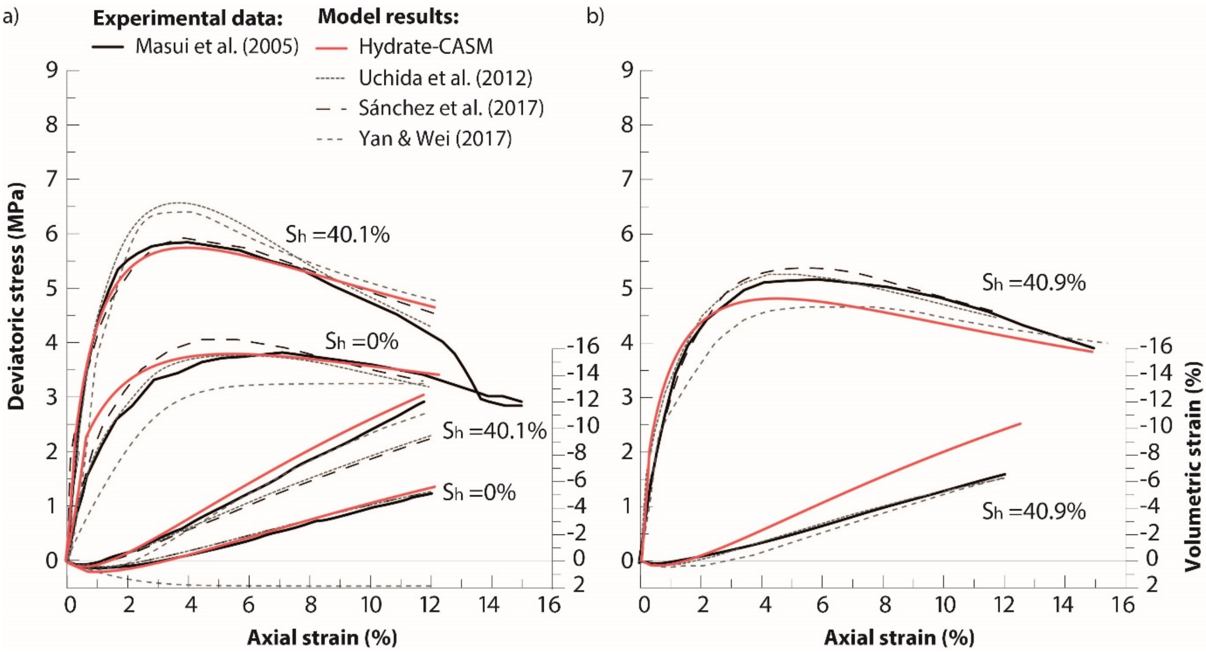

Figure 10: Model comparison between Hydrate-CASM predictions and those obtained from, Uchida et al. [39], Sánchez et al. [41] and Yan & Wei [50] models against the experimental data from [19]. The results are presented in terms of stress-strain relationship and volumetric behavior for (a) cementing and (b) pore-filling specimens.

4.2. Modeling of Hyodo's et al. (2013) experimental tests

Hyodo et al. [21] performed a series of triaxial tests to investigate the mechanical properties and dissociation characteristics of synthetic MHBS. They used an innovative temperature controlled high-pressure apparatus specially developed to reproduce the in-situ conditions expected during gas extraction from hydrates. Three sets of triaxial tests conducted at zero or constant hydrate saturation are used here for the model application. The tests were performed on Toyoura sand with an initial porosity of about 40% (e ≈0.65), subjected to confining effective stress of 1, 3 and 5 MPa with different hydrate saturations. The experimental data from the sediments without hydrate are used to calibrate the critical state parameters of the model (Table 5) and those from the hydrate-bearing sand are used to examine the model capability at capturing the mechanical effect of S_h.

Table 5. Input parameters for modelling Hyodo's et al. [21] triaxial tests at 1, 3 and 5 MPa of confining effective stress.

Model parameters									
e	λ	M	$p'_0(MPa)$	κ	υ	n	r	$p'_{0_s}(MPa)$	u
0.65	0.22	1.32	9	0.015	0.1	4	2.5	5.6	50

Figure 11 shows the simulation of the experimental tests performed by Hyodo et al. [21]. The results show the capability of the Hydrate-CASM at capturing changes in the mechanical response of the host sediment with increasing confining effective stress. For the host sediment confined at 1 MPa the model predicts a moderate softening after a peak and the volumetric strain goes from compressive to slightly dilatant (S_h=0%, Figure 11a). With increasing effective stress, the model predicts a gradual transition of this response towards a hardening and a fully contracting behavior, although the maximum deviatoric stress at 3 and 5 MPa are slightly underestimated (S_h=0%; Figure 11c and 11e). The results for the hydrate-bearing sand show, in general, a good agreement with the experimental data, capturing both the trend and magnitude of the stress-strain and volumetric responses of the sediment (Figure 11a, c and 11e) and the $e - \ln(p')$ paths during triaxial shear (Figure 11b, 11d and 11f). However, the model largely overestimated the peak strength for the sediment with S_h = 53.7% tested at 3 MPa (Figure 11c).

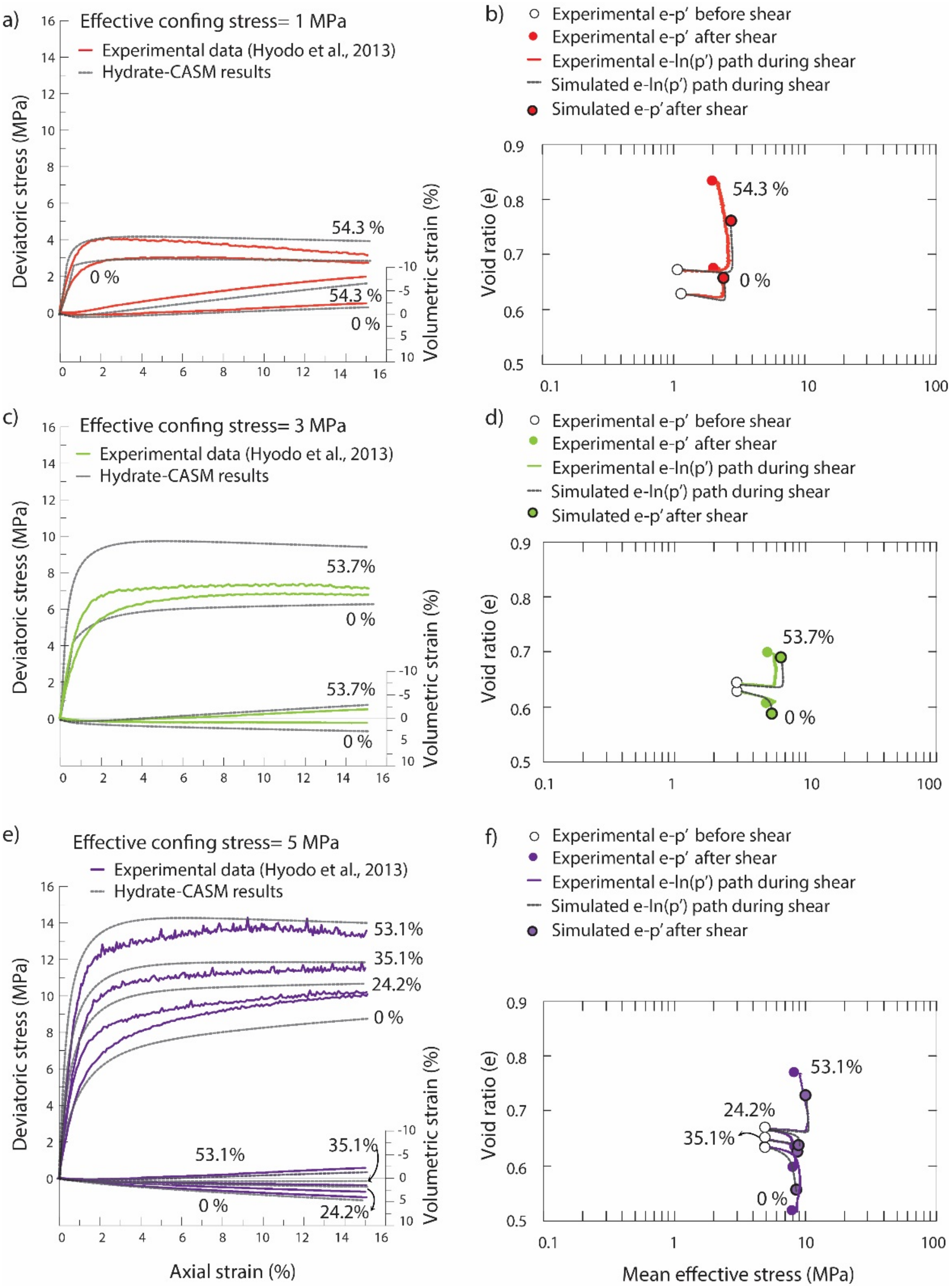

Figure 11: Modelling of Hyodo's et al. [21] experimental data. Results are presented in terms of deviatoric stress-axial strain, volumetric strain-axial strain and void ratio-mean effective stress relationships at effective confining stress of (a, b) 1 MPa, (c, d) 3 MPa, and (e, f) 5 MPa. For comparison purposes, the $e - ln\ (p')$ paths during triaxial shear are adjusted to the potential void ratio reported by Hyodo et al. [21] after isotropic consolidation. Percentages indicated in the figure correspond to hydrate saturations.

The maximum strength of the sediments examined in this section tends to increase almost linearly with hydrate saturation. However, the sediment with S_h = 53.7% does not follow this trend (Figure 12a). Hyodo et al. [21] estimated the hydrate saturation within the sediment based on the stoichiometry of the hydrate formation reaction and assuming that all the methane gas injected converted into hydrate. Several studies have proposed that hydrate and gas can coexist under hydrate stability conditions [76-78]. In particular, Sahoo et al. [79] show experimental evidence in which hydrate formation stops with up to 13% of gas still on the sediment under favorable pressure, temperature and salinity conditions. Accordingly, we hypothesize that is possible that part of the gas injected into the specimen with S_h=53.7% could not form hydrate and consequently, the saturation reported could have been slightly overestimated. For comparison purposes, the same test was modelled considering S_h= 24.2%, which is a more consistent value within the linear $q_{max} - S_h$ trend observed for the rest of the experimental data (Figure 12a). Considering S_h= 24.2%, the Hydrate-CASM reproduces closely the deviatoric stress-axial strain relationship reported experimentally (Figure 12b).

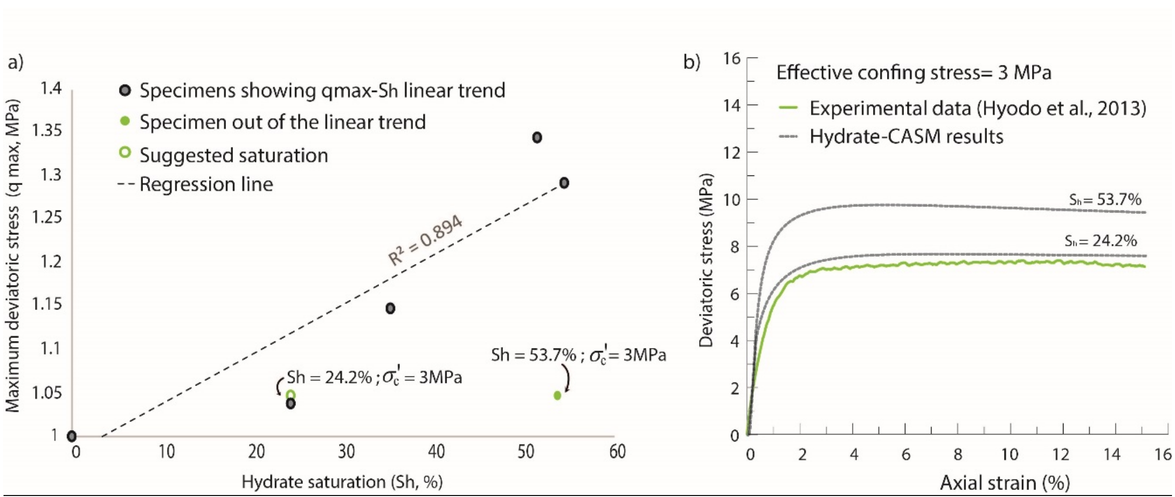

Figure 12: Effect of hydrate saturation on the peak strength of MHBS. (a) $q_{max} - S_h$ relatively linear trend for Hyodo's et. al. [21] experimental data. Note that the maximum deviatoric stress is normalized by the value reported in the corresponding sediment without hydrate. (b) Model predictions considering both S_h=53.7% and S_h=24.2% for the sediment confined at 3MPa.

The results presented in this section have been validated against the outputs from three other mechanical models for MHBS [41, 48, 49] (Figure 13). The comparison is satisfactory and shows that, despite the simplicity of the densification mechanism, the Hydrate-CASM performs similarly to models that require more than one hydrate-related empirical parameters in their formulation.

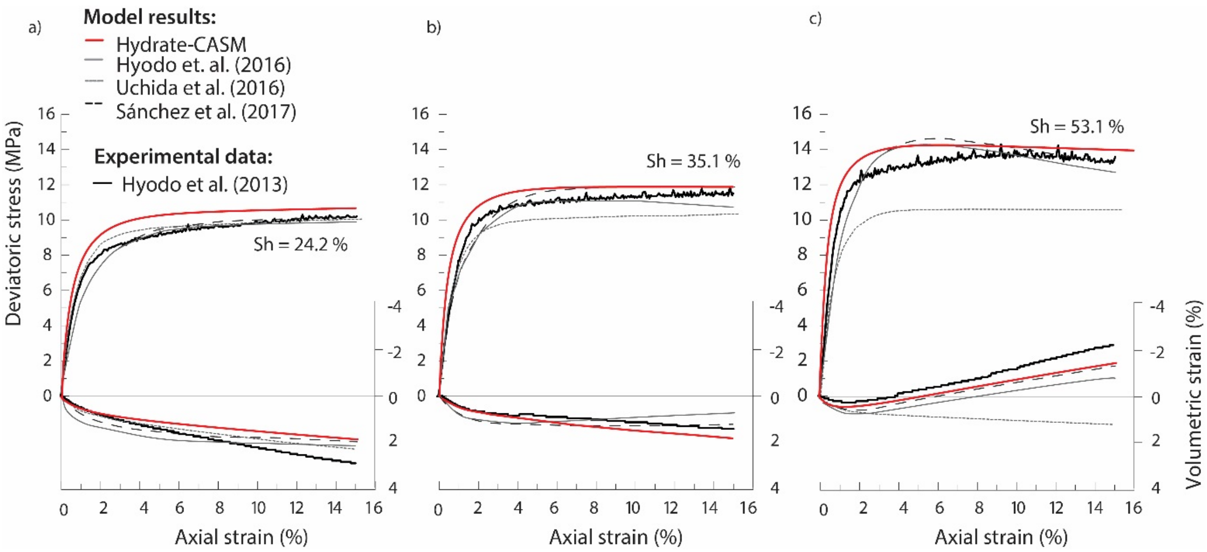

Figure 13: Model comparison between the results from Hydrate-CASM, Sánchez et al. [41] Hyodo et. al. [48], Uchida et al. [49] models against the experimental data from Hyodo et al. [21]. Stress-strain behavior and volumetric response for hydrate-bearing sediments with (a) S_h=24.2%, (b) S_h=35.1% and (c) S_h=53.1% subjected to triaxial shear under confining effective stress of 5 MPa.

5. CONCLUSIONS

The Hydrate-CASM is a new elastoplastic constitutive model developed to simulate the mechanical behavior of MHBS. This model extends the formulation of the CASM model by implementing the subloading surface model and introducing the densification mechanism. Alternatively to bonding or cementing models, the Hydrate-CASM suggests that the greater strength and dilatancy observed in MHBS can be explained by the densification and stiffening effects that pore invasion with hydrate has on the mechanical properties of the sediment. The densification mechanism attributes hydrate-related changes in the host sediment available void ratio, swelling line slope and isotropic yield stress to sediment stress-strain changes. Moreover, the flexibility in the shape of the Hydrate-CASM yield function and the use of a non-associated flow rule make our formulation particularly suitable for modelling the behavior of sands, the most likely target deposit for commercial exploitation of hydrates.

Compared to previous models for MHBS, our formulation reduces to one the number of empirical hydrate-dependent parameters required to reasonably capture the mechanical behavior of MHBS. Our formulation only requires an empirical hydrate-dependent parameter to account for changes in the swelling line slope with hydrate saturation. Reducing to one the number of these parameters is an important advance in mechanical constitutive modeling of MHBS (i) because obtaining them through laboratory tests is challenging, especially if their physical meaning is not well understood, and (ii) because eases the application of the Hydrate-CASM model to a wide range of experimental test conditions.

Robust and well-described published experimental tests have been chosen to calibrate the Hydrate-CASM capabilities at modelling the mechanical behavior of MHBS during triaxial shear. These tests cover the most relevant conditions related to MHBS behavior, including a wide range of hydrate saturations, several hydrate morphologies and confinement stress. In addition, they have been previously used to calibrate other mechanical models developed for MHBS, which allowed us to compare and validate our results. Our simulations evidence the ability of the Hydrate-CASM to predict both stress-strain and the volumetric response of synthetic MHBS subjected to triaxial shear and suggest that quantifying the void ratio and the mechanical response of the host sediment is key to isolate hydrate-related mechanical contributions.

6. ACKNOWLEDGEMENT

The authors thank the constructive and thoughtful comments of three anonymous reviewers that have helped to improve this article. Maria De La Fuente was supported by the Graduate School of the National Oceanography Centre Southampton.

7. REFERENCES

1. Holder G.D., Kamath, V.A., and S.P. Godbole. The potential of natural gas hydrates as an energy resource, Annual Review of Energy 1984; 9, 427-445.
2. Grauls, D. Gas hydrates: Importance and applications in petroleum exploration. Mar. Pet. Geol. 2001; 18, 519 – 523.
3. Collett, T. S. Energy resource potential of natural gas hydrates, AAPG Bull. 2002; 86(11), 1971–1992.

4. Dallimore, S R, and Collett, T S. Summary and implications of the Mallik 2002 Gas Hydrate Production Research Well Program. In Scientific results from the Mallik 2002 Gas Hydrate Production Research Well Program, Mackenzie Delta, Northwest Territories, Canada (eds S. R. Dallimore & T. S. Collett), , 2005 Bulletin 585. Ottawa, Ontario: Geological Survey of Canada.
5. Ruppel, C. Tapping methane hydrates for unconventional natural gas, Elements 2007; 3, 193 – 199.
6. Nagel, N. Compaction and subsidence issues within the petroleum industry: From wilmington to ekofisk and beyond. Physics and Chemistry of the Earth 2001; Part A: Solid Earth and Geodesy 26(1-2), 3–14. 7.
7. Freij-Ayoub, R., Tan, C., Clennell, B., Tohidi, B., and Yang, J. A wellbore stability model for hydrate bearing sediments. Journal of Petroleum Science and Engineering 2007; 57(1–2), 209–220.
8. Yamamoto, K., and Dallimore, S. Aurora-JOGMEC-NRCan Mallik 2006- 2008 Gas Hydrate Research Project Progress. Fire in Ice, Methane Hydrate Newsletter, National Energy Technology Laboratory 2008; 8, 1–20.
9. Dickens, G. R., O'Neil, J. R., Rea, D. K., and Owen, R. M. Dissociation of oceanic methane hydrate as a cause of the carbon isotope excursion at the end of the Paleocene, Paleoceanography 1995; 19, 965–971.
10. Archer, D. Methane hydrate stability and anthropogenic climate change. Biogeosciences 2007; 4, 521–544.
11. Ruppel, C., and J. W. Pohlman. Climate change and the global carbon cycle: Perspectives and opportunities, Fire in the Ice: Methane Hydrate Newsletter 2008; winter, pp. 5 – 8, Off. of Fossil Energy, Natl. Energy Technol. Lab., U.S. Dep. of Energy, Washington, D. C.
12. Minshull, T. A., Marín-Moreno, H., Armstrong McKay, D. I., and Wilson, P. A. Mechanistic insights into a hydrate contribution to the Paleocene-Eocene carbon cycle perturbation from coupled thermohydraulic simulations. Geophysical Research Letters 2016; 43(16), 8637–8644.
13. Sultan, N., P. Cochonat, J. P. Foucher, and J. Mienert. Effect of gas hydrates melting on seafloor slope instability, Mar. Geol. 2004; 213, 379– 401.
14. Pecher, I. a., Henrys, S. a., Ellis, S., Chiswell, S. M. and Kukowski, N. Erosion of the seafloor at the top of the gas hydrate stability zone on the Hikurangi Margin, New Zealand. Geophysical Research Letters 2005; 32(24), 3–6.
15. Paull, C. K., Ussler, W., Dallimore, S. R., Blasco, S. M., Lorenson, T. D., Melling, H., Medioli, B. E., Nixon, F. M. & McLaughlin, F. A. Origin of pingo-like features on the Beaufort Sea shelf and their possible relationship to decomposing methane gas hydrates. Geophysical Research Letters 2007; 34(1), 1–5.
16. Priest, J. A. A laboratory investigation into the seismic velocities of methane gas hydrate-bearing sand. Journal of Geophysical Research 2005; 110(B4), 1–13.
17. Winters, W., Waite, W., Mason, D., Gilbert, L. and Pecher, I. Methane gas hydrate effect on sediment acoustic and strength properties. Journal of Petroleum Science and Engineering 2007; 56(1-3), 127–135.
18. Priest, J. A., Rees, E. V. L. & Clayton, C. R. I. Influence of gas hydrate morphology on the seismic velocities of sands. Journal of Geophysical Research 2009; 114(B11), 1–13.
19. Masui, A., H. Haneda, Y. Ogata, and K. A. The effect of saturation degree of methane hydrate on the shear strength of synthetic methane hydrate sediments, Proceedings of the 5th International Conference on Gas Hydrates, Trondheim, Norway 2005; vol. 2037, pp. 657–663.

20. Miyazaki, K., Masui, A., Sakamoto, Y., Aoki, K., Tenma, N., and Yamaguchi, T. Triaxial compressive properties of artificial methane-hydrate-bearing sediment. Journal of Geophysical Research: Solid Earth 2011; 116(6), 1–11.
21. Hyodo, M., Yoneda, J., Yoshimoto, N., and Nakata, Y. Mechanical and dissociation properties of methane hydrate-bearing sand in deep seabed. Soils and Foundations 2013; 53(2), 299–314.
22. Soga, K., S. L. Lee, M. Y. A. Ng, and A. Klar. Characterisation and engineering properties of methane hydrate soils, Characterization and Engineering Properties of Natural Soils 2006; vol. 4, edited by K. Soga et al., pp. 2591–2642, Taylor and Francis, London, U. K.
23. Waite, W. F., Santamarina, J. C., Cortes, D. D., Dugan, B., Espinoza, D. N., Germaine, et al. Physical Properties of Hydrate-Bearing Sediments. Rev. Geophys 2009; 47, RG4003.
24. Hannegan, D., Todd, R. J., Pritchard, D. M. & Jonasson, B. Uniquely Applicable to Methane Hydrate Drilling. In: SPE/IADC Underbalanced Technology Conference and Exhibition. Houston, USA 2004.
25. McIver, R. D. Role of naturally occurring gas hydrates in sediment transport. The American Association of Petroleum Geologist Bulletin 1982; 66(6), 789–792.
26. Kayen, R.E., and Lee, H.J. Slope stability in regions of sea-floor gas hydrate; Beaufort Sea continental slope, in Schwab, W.C. 1993.
27. Nixon, M. F., and J. L. H. Grozic. Submarine slope failure due to gas hydrate dissociation: A preliminary quantification. Can. Geotech. J. 2007; 44, 314–325
28. Borowski, W. S. & Paul, C. K. The Gas Hydrate Detection Problem: Recognition of Shallow-Subbottom Gas Hazards in Deep-Water Areas. In: Off-shore Technology Conference. Houston, USA, 1997: Offshore Technology Conference.
29. Chaouachi, M., Falenty, A., Sell, K., Enzmann, F., Kersten, M., Haberthur, D., and Kuhs, W. Microstructural evolution of gas hydrates in sedimentary matri-ces observed with synchrotron x-ray computed tomographic microscopy. Geochem.Geophy. Geosy. 2015, 16:1711–1722.
30. Sahoo, S. K., Madhusudhan, B. N., Marin-Moreno, H., North, L. J., Ahmed, S., Falcon-Suarez, I., and Best, A. Laboratory insights into the effect of sediment-hosted methane hydrate morphology on elastic wave velocity from time lapse 4D synchrotron X-ray computed tomography. Geochemistry, Geophysics, Geosystems. 2018, 19(11):4502–4521.
31. Sell, K., Saenger, H., Quintal, B., and Enzmann, F., K. M. Digital lab of hydrate-bearing sediments: Determination of effective elastic properties on the microscale. European Geosciences Union - General Assembly 2017
32. Pinkert, S. Rowe’s Stress-Dilatancy Theory for Hydrate-Bearing Sand. International Journal of Geomechanics 2016; 17(1), 6016008.
33. Pinkert, S. The lack of true cohesion in hydrate-bearing sands. Granular Matter. 2017; 19. 10.1007/s10035-017-0742-5.
34. Pinkert, S., and Grozic, J. L. H. Experimental verification of a prediction model for hydrate bearing sand. Journal of Geophysical Research: Solid Earth 2016; (October).
35. Klar, A., Soga, K., and Ng, M. Y. a. Coupled deformation–flow analysis for methane hydrate extraction. Géotechnique 2010; 60(10), 765–776.

36. Jung, J. W., Santamarina, J. C., and Soga, K. Stress-strain response of hydrate-bearing sands: Numerical study using discrete element method simulations. Journal of Geophysical Research: Solid Earth 2012; 117(4), 1–12.
37. Pinkert, S., and Grozic, J. L. H. Prediction of the mechanical response of hydrate-bearing sands, Journal of Geophysical Research: Solid Earth 2014; 4695–4707.
38. Pinkert, S., Grozic, J. L. H., and Priest, J. A. Strain-Softening Model for Hydrate-Bearing Sands. International Journal of Geomechanics 2015, 15(6), 1–6.
39. Uchida, S., Soga, K., and Yamamoto, K. Critical state soil constitutive model for methane hydrate soil, Journal of Geophysical Research: Solid Earth 2012, 117(B3).
40. Sánchez, M., and Gai, X. Geomechanical and numerical modeling of gas hydrate sediments. Energy Geotechnics 2016, 19–24.
41. Sánchez, M., Gai, X., and Santamarina, J. C. A constitutive mechanical model for gas hydrate bearing sediments incorporating inelastic mechanisms. Computers and Geotechnics 2017; 84, 28–46.
42. Sultan, N., and Garziglia, S. Geomechanical constitutive modelling of gas-hydrate bearing sediments. The 7th International Conference on Gas Hydrates, (ICGH) 2011.
43. De La Fuente, M., Vaunat, J., and Marín-Moreno, H. Composite model to reproduce the mechanical behaviour of Methane Hydrate Bearing Sediments. Energy Geotechnics 2016; 483–489.
44. Jiang, M., Zhu, F., Liu, F., and Utili, S. (2014). A bond contact model for methane hydrate-bearing sediments with interparticle cementation. International Journal for Numerical and Analytical Methods in Geomechanics 2014; 38(17), 1823–1854.
45. Lin, J.S., Seol, Y. and Choi, J. H. An SMP critical state model for methane hydrate-bearing sands. International Journal for Numerical and Analytical Methods in Geomechanics 2015; 32(9), 969–987.
46. Yu, H. S. CASM: a unified state parameter model for clay and sand. International Journal for Numerical and Analytical Methods in Geomechanics 1998; 22(8), 621–653.
47. Hashiguchi, K. Subloading surface model in unconventional plasticity. Int. J. Solids Struct. 1989; 25(8), 917–945.
48. Hyodo, M., Nakata, Y., and Yoshimoto, N. Challenge for methane hydrate production by geotechnical engineering. Proceeding of the 15th Asian Regional Conference on Soil Mechanics and Geotechnical Engineering 2016; 62–75.
49. Uchida, S., Xie, X.-G. and Leung, Y.F. Role of critical state framework in understanding geomechanical behaviour of methane hydrate-bearing sediments, Journal of Geophysical Research 2016; 121(8), 5580-5595
50. Yan, R., and Wei, C. Constitutive Model for Gas Hydrate–Bearing Soils Considering Hydrate Occurrence Habits. International Journal of Geomechanics 2017; 17(8), 4017032.
51. Boswell R, Collett TS. Current perspectives on gas hydrate resources. Energy & Environmental Science 2011; 4:1206–1215.
52. Been, K. and Jefferies, M. G.. A state parameter for sands. Géotechnique 1985, 35(2), 99-112.
53. Graham, J., Crooks, J. H. A., and Bell, A. L Time effects on the stress-strain behaviour of natural soft clays. Geotechnique. 1983; 33(3),327–340
54. Lade, B. P. V, and Nelson, R. B. Non-Associated flow and stability of granular materials. J. Eng. Mech,1988; 113(9), 1302–1318.

55. Roscoe, K. H., A. N. Schofield, and C. P. Wroth. On the yielding of soils, Geotechnique 1958, 8(1), 22–53.
56. Roscoe, K. H., and J. B. Burland. On the generalized stress-strain behaviour of wet clays, in Engineering Plasticity. Edited by J. Heyman and F. A. Leckie 1968, Pp. 535–609, Cambridge Univ. Press, Cambridge, England.
57. Nova, R. and Wood, D. M. An experimental program to define yield function for sand, Soils and Foundations 1978, 18(4),77-86.
58. Chandler, H. W. A plasticity theory without Drucker's postulate for granular materials. J. Mech. Phys. Solids 1985, 33, 215-226.
59. Rowe, P. W. The stress-dilatancy relation for static equilibrium of an assembly of particles in contact. Proc. Roy. Soc. 1962; 267, 500-527.
60. Jardine, R. J. Some observations on the kinematic nature of soil stiffness. Soils Found. 1992; 32(2), 111–124.
61. Mitchell, J. K., and Soga K. Fundamentals of Soil Behaviour. John Wiley, Hoboken, N.J. 2005.
62. González, N. Development of a family of constitutive models for geotechnical applications. PhD thesis, Polytechnic University of Catalonia, Barcelona (Spain), (May) 2011.
63. Vialle, S. and Vanorio, T. Laboratory measurements of elastic properties of carbonate rocks during injection of reactive CO2-saturated water. Geophysical Research Letters 2011; 38. L01302
64. Nygaard, R., Bjørlykke, K., Høeg, K., Hareland, G. The effect of diagenesis on stress-strain behavior and acoustic velocities in sandstones. Proceedings of the 1st Canada-US Rock Mechanics Symposium - Rock Mechanics Meeting Society's Challenges and Demands 2007.
65. Pinyol Puigmartí, NM., Vaunat, J., Alonso Pérez de Agreda, E. A constitutive model for soft clayey rocks that includes weathering effects. Geotechnique 2007;57 (2):137–51.
66. Chagneau, A., Claret, F., Enzmann, F., Kersten, M, Heck, S., et al.. Mineral precipitation-induced porosity reduction and its effect on transport parameters in diffusion-controlled porous media. Geochemical Transactions, Chemistry Central, 2015, 16 (1), 16 p.
67. Gupta, S., Helmig, R. and Wohlmuth, B. Non-isothermal, multi-phase, multi-component flows through deformable methane hydrate reservoirs. Computational Geosciences. 2015; 19. 1063-1088. 10.1007/s10596-015-9520-9.
68. Yoneda, J., Oshima, M., Kida, M., Kato, A., Konno, Y., Jin, Y., Tenma, N. Consolidation and hardening behavior of hydrate-bearing pressure-core sediments recovered from the Krishna–Godavari Basin, offshore India, Marine and Petroleum Geology. 2018, ISSN 0264-8172.
69. Masui, A., H. Haneda, Y. Ogata, and K. A. Mechanical properties of sandy sediment containing marine gas hydrates in deep sea offshore Japan survey drilling in Nankai Trough. In Proceedings of Seventh ISOPE Ocean Mining Symposium, pp. 53–56, International Society of Offshore and Polar Engineers 2007, Lisbon, Portugal.
70. Lu, W., I. M. Chou, and R. C. Burruss. Determination of methane concentrations in water in equilibrium with sI methane hydrate in the absence of a vapor phase by in situ Raman spectroscopy. Geochim. Cosmochim. Acta 2008; 72, 412–422.
71. Lee, J. Y., Santamarina, J. C., and Ruppel, C. Volume change associated with formation and dissociation of hydrate in sediment. Geochemistry, Geophysics, Geosystems 2010, 11(3).

72. Hyodo, M., Kajiyama S., Yoshimoto, N., Nakata, Y. Triaxial behaviour of methane hydrate bearing sand. Proceedings of 10th Int. ISOPE Ocean Mining & Gas Hydrate Symposium OMS-2013, Szczecin, Poland, 2014; 126-134.
73. Santamarina, J.C.; Dai, S.; Terzariol, M.; Jang, J.; Waite, W.F.; Winters, W.J.; Nagao, J.; Yoneda, J.; Konno, Y.; Fujii, T.; et al. Hydro-bio-geomechanical properties of hydrate-bearing sediments from Nankai Trough. Mar. Pet. Geol. 2015; 66, 1–17.
74. Song, Y.C.; Zhu, Y.M.; Liu, W.G.; Li, Y.H.; Lu, Y.; Shen, Z.T. The effects of methane hydrate dissociation at different temperatures on the stability of porous sediments. Journal of Petroleum Science and Engineering 2016; 147(May), 77–86.
75. Hyodo, M., Li, Y., Yoneda, J., Nakata, Y., Yoshimoto, N., Nishimura, A. Effects of dissociation on the shear strength and deformation behavior of methane hydrate-bearing sediments, Marine and Petroleum Geology. 2014, Volume 51, Pages 52-62, ISSN 0264-8172.
76. Milkov, A. V. Global estimates of hydrate-bound gas in marine sediments: how much is really out there? Earth-Sci. Rev. 2004; 66, 183– 197.
77. Darnell, K. N., and P. B. Flemings. Transient seafloor venting on continental slopes from warming-induced methane hydrate dissociation. Geophys. Res. Lett. 2015; 42, 10765–10772.
78. Goswami, B. K., K. A. Weitemeyer, T. A. Minshull, M. C. Sinha, G. K. Westbrook, A. Chabert, T. J. Henstock, and S. K. A joint electromagnetic and seismic study of an active pockmark within the hydrate stability field at the Vestnesa Ridge, West Svalbard margin. J. Geophys. Res. Solid Earth 2015; 120, 6797–6822.
79. Sahoo, S., Marín-Moreno, H., North, L., Falcon-Suarez, I. Bn, M., Best, A. and Minshull, T. Presence and Consequences of Coexisting Methane Gas With Hydrate Under Two Phase Water-Hydrate Stability Conditions. Journal of Geophysical Research: Solid Earth.2018; 10.1029/2018JB015598.